J. Phys. Chem. A **2006,** *110,* 8467−8476

Two-Channel Dissociation of Chemically and Thermally Activated *n*-Butylbenzene Cations ($C_{10}H_{14}^+$)[†]

Abel I. Fernandez,[‡,§] A. A. Viggiano,*[,‡] and J. Troe[||]

Air Force Research Laboratory, Space Vehicles Directorate, 29 Randolph Rd., Hanscom AFB, Massachusetts 01731-3010, and Institute for Physical Chemistry, University of Goettingen, Tammannstrasse 6, D-37077 Goettingen, Germany

Received: November 25, 2005; In Final Form: January 20, 2006

The charge-transfer reaction $O_2^+ + n$-butylbenzene ($C_{10}H_{14}$) → $O_2 + C_{10}H_{14}^{+*}$ was studied in a turbulent ion flow tube at temperatures between 423 and 548 K and pressures between 15 and 250 Torr in the buffer gases He and N_2. Under chemical activation conditions stabilization vs dissociation ratios *S/D* of vibrationally highly excited $C_{10}H_{14}^{+*}$ as well as branching ratios of the fragments $C_7H_7^+$ ($m/z = 91$) vs $C_7H_8^+$ ($m/z = 92$) of the dissociation of $C_{10}H_{14}^{+*}$ were measured. Under thermal activation conditions, the rate constant of the dominating dissociation channel 92 was measured at 498 and 523 K. Employing information on the specific rate constants $k(E)$ of the two channels 91 and 92 and on collisional energy transfer rates from the literature, the measured *S*/*D* curves and branching ratios 91/92 could be modeled well. It is demonstrated that the charge transfer occurs approximately equally through resonant transfer and complex-forming transfer. The thermal dissociation experiments provide a high precision value of the energy barrier for the channel 92, being 1.14 (±0.02) eV.

1. Introduction

The dissociation of *n*-butylbenzene cations ($C_{10}H_{14}^+$) serves as a prototype for ion dissociations which proceed with competing channels[1] and for which the specific rate constants $k_i(E)$ of the channels *i* could be established by absolute[2,3] and relative[2−15] rate measurements. At low energies, the two channels

$$C_{10}H_{14}^+ \rightarrow C_7H_7^+ + C_3H_7 \ (m/z = 91) \qquad (1.1)$$

$$\rightarrow C_7H_8^+ + C_3H_6 \ (m/z = 92) \qquad (1.2)$$

dominate the reaction. Process 1.2 involves a McLafferty rearrangement with a reverse barrier,[2] and process 1.1 forms benzylium ions by a simple bond fission without a reverse barrier. Process 1.1 may also produce tropylium ions in either a direct process with a reverse barrier or in a secondary process by isomerization of vibrationally highly excited benzylium ions formed in reaction 1.1. The latter was investigated in a study of the dissociation of ethylbenzene cations.[16] The tropylium channel was found to be more important in smaller alkylbenzenes cation dissociations than in *n*-butylbenzene cation dissociation.[16,23] The specific rate constants $k_{92}(E)$ of reaction 1.2 have been determined in absolute rate measurements by the photoelectron−photoion coincidence (PEPICO) technique in the milli- to microsecond time range[2] and by photodissociation mass analyzed ion kinetic energy spectrometry (PD-MIKES) in the nanosecond time range.[3] In addition, the branching ratio of the specific rate constants $k_{91}(E)/k_{92}(E)$ (also denoted by 91/92) was measured by a variety of techniques[2−15] and has served as a “molecular thermometer”[2,12] allowing one to establish the internal energy *E* of $C_{10}H_{14}^+$. Combining the absolutely measured $k_{92}(E)$ with the branching ratio $k_{91}(E)/k_{92}(E)$ directly leads to the specific rate constant $k_{91}(E)$ of reaction 1.1. Both $k_{91}(E)$ and $k_{92}(E)$ have been modeled by standard rigid activated complex Rice−Ramsperger−Kassel−Marcus (RRKM) theory, which provided estimates of the kinetic shifts of single[2,3,15] and competing channels[15] of the reaction, which led to values of the threshold energies $E_0(91)$ and $E_0(92)$ of reactions 1.1 and 1.2, respectively. Threshold collision-induced dissociation (TCID) measurements were made on the reaction system[15] as well, to determine the threshold energies of reactions 1.1 and 1.2. In ref 17, RRKM theory was superseded by statistical adiabatic channel model/classical trajectory (SACM/CT) calculations for the bond fission (1.1) where a fixed rigid activated complex loses its significance. The SACM/CT calculations allowed for a new determination of kinetic shifts and hence of the threshold energy $E_0(91)$ of reaction 1.1.[17]

The availability of specific rate constants $k_{91}(E)$ and $k_{92}(E)$ over wide energy ranges also allows one to study reactions 1.1 and 1.2 under more general conditions and to test a variety of methods for the analysis of rate parameters under less energy-specific conditions than applied in refs 2 and 3. This is the issue of the present work, in which chemically and thermally activated *n*-butylbenzene cations were produced and reacted to form the competing channels 1.1 and 1.2. In chemical activation experiments, vibrationally highly excited butylbenzene cations, $C_{10}H_{14}^{+*}$, were formed by the charge exchange process

$$O_2^+ + C_{10}H_{14} \rightarrow O_2 + C_{10}H_{14}^{+*} \qquad (1.3)$$

The use of our turbulent ion flow tube (TIFT) technique[16,18−23] allowed us to employ sufficiently high pressures of a buffer gas (in the 15−300 Torr range) such that $C_{10}H_{14}^{+*}$ could be stabilized (*S*) in competition with dissociation (*D*) via channels 1.1 and 1.2. Measurements of the ratio *S*/*D* provide information on the stabilization rate if one can rely on the measurements of

---

[†] Part of the “Chava Lifshitz Memorial Issue”.

* Corresponding author. E-mail: albert.viggiano@hanscom.af.mil.

[‡] Air Force Research Laboratory.

[||] Institute for Physical Chemistry, University of Goettingen.

[§] National Academy of Sciences Postdoctoral Fellow.

10.1021/jp056846c CCC: $33.50

the dissociation rates described above. In particular, if the total rate coefficient for energy transfer between $C_{10}H_{14}^{+*}$ and the buffer gas M can be identified with the collision frequency Z, one may determine the average energy $\langle \Delta E \rangle$ transferred per collision. We have described experiments of this type for highly vibrationally excited ethylbenzene and *n*-propylbenzene cations in refs 22 and 23, respectively. Since only a small amount of information on $\langle \Delta E \rangle$ is available for molecular ions (from relative rate measurements such as described in refs 24−27), it appears worthwhile to perform S/D measurements on *n*-butylbenzene cations as well.

It was suggested in refs 22 and 23 that charge exchange (1.3) proceeds by three mechanisms. A resonant process produces $C_{10}H_{14}^{+*}$ with an energy equal to the ionization potential difference between $C_{10}H_{14}$ and O_2 plus the vibrational energy of $C_{10}H_{14}$. The second process involves a bound $(O_2{-}C_{10}H_{14})^+$ intermediate complex which statistically partitions vibrational energy between O_2 and $C_{10}H_{14}^+$ upon dissociation such that $C_{10}H_{14}^{+*}$ contains less vibrational energy (and in a different distribution) than in the resonant process. Finally, electronically excited $O_2(^1\Delta_g)$ or $O_2(^1\Sigma_g^+)$ may be produced, such that $C_{10}H_{14}^{+*}$ contains even less vibrational energy. The present study of the *n*-butylbenzene cation system tests the hypothesis of several charge-transfer pathways.

At sufficiently high pressures, thermally activated $C_{10}H_{14}^+$ ions can be generated[23,28,29] after collisional stabilization of chemically activated $C_{10}H_{14}^{+*}$ from reaction 1.3. If the temperatures are high enough, collisional stabilization and thermalization of $C_{10}H_{14}^{+*}$ is followed by thermal dissociation on a much longer time scale. Our earlier studies of ethylbenzene$^+$ and *n*-propylbenzene$^+$ pyrolysis have indicated that these reactions were in the high-pressure range of unimolecular dissociation.[28] One may safely assume analogous behavior for the dissociation of *n*-butylbenzene cations under the same high-pressure conditions. Our measurements of the thermal dissociation rates of *n*-butylbenzene cations are therefore complementary to the studies of dissociations of the energy-selected ions. In particular, literature values of the threshold energy $E_0(92)$ of reaction 1.2 vary substantially. These can be tested by analyzing our measured absolute value of the thermal dissociation rate constant since it very sensitively depends on $E_0(92)$.

A further point of interest is to measure the branching ratio 91/92 in both chemical and thermal activation experiments and analyze it in terms of the ratios $k_{91}(E)/k_{92}(E)$ from the detailed energy-specific measurements mentioned above. Like in earlier work, this ratio can serve as a molecular thermometer. In the present case, it allows us to deduce the relative importance of the different charge-transfer mechanisms for reaction 1.3 described above. Finally, the formation of a minor fragment at $m/z = 105$, possibly arising from a process[15]

$$C_{10}H_{14}^+ \rightarrow C_8H_9^+ + C_2H_5 \qquad (1.4)$$

was studied under chemical activation conditions.

There is a practical nature to these studies. They contribute to a better understanding of the reactions of aromatic fuels with air plasma ions such as O_2^+ and NO^+ and their subsequent reactions.[16,18,22,23,30,31] These processes play a role in advanced hydrocarbon-fueled air breathing propulsion systems[29,32] wherein combustion is required to occur on short time scales. It has been found that ionization enhances combustion by shortening ignition delays. The present study adds detailed kinetic information on the ion−molecule reactions involved. This information has been lacking, especially at the higher pressures and temperatures that are relevant to studies of combustion systems. The present work allows for extrapolations to be made to the relevant conditions.

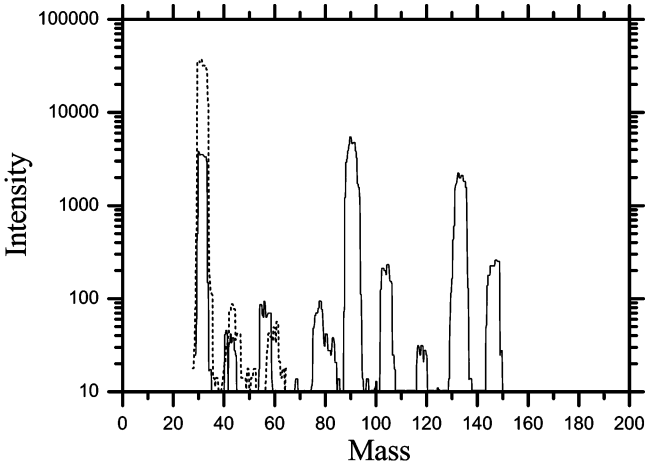

Figure 1. Typical low-resolution mass spectrum of the $O_2^+ + C_{10}H_{14}$ system. The dashed peak at mass 32 corresponds to the undepleted O_2^+ signal before the addition of *n*-butylbenzene. The peak at mass 147 corresponds to secondary reaction of benzylium ($C_7H_7^+$) with $C_{10}H_{14}$, see eq 2.1.

2. Experimental Technique and Results

Our experiments were conducted in the turbulent ion flow tube (TIFT) which has been described in detail before;[18,19,29] therefore, the technique is only briefly summarized here. The TIFT is similar to low-pressure flow tubes except that larger flow rates are used to achieve higher pressures and Reynolds numbers. A liquid nitrogen storage vessel supplies the N_2 carrier gas, which is preheated in a sidearm. A few experiments were made in a helium buffer using bottled high purity helium scrubbed in liquid-nitrogen-cooled molecular sieve traps. The precursor ions, O_2^+, are created upstream in an off-axis corona discharge source and are entrained into the N_2 or He flow in the sidearm. The bulk flow enters the flow tube where a gas mixture of N_2 and vapor of the neutral reagent *n*-butylbenzene is injected through a moveable, on-axis tube; this promotes efficient charge transfer to produce *n*-butylbenzene cations. At the end of the flow tube, most of the gas is removed by a large mechanical pump while a small fraction is sampled through a 150 μm orifice in a truncated nosecone. The core of the ensuing supersonic expansion is sampled through a skimmer into a mass spectrometer. The ions are analyzed by a quadrupole mass filter and counted by a discrete dynode electron multiplier.

To elevate the temperature, five zones of heating are used, and the thermocouple that monitors the gas temperature is maintained to ±2 K. The main flow tube is heated in three zones: one short zone at the upstream end near the bellows, a long middle section, and a zone inside the vacuum chamber just upstream of the nosecone. The connection between the corona discharge tube and the sidearm is also heated. Finally, it was found that preheating of the buffer gas is needed since the residence time is too small to cope with the decrease in heat transfer which in turn is due to high pressures. The preheater consists of two Mellen split type (clam shell) tubular heating elements that surround a tubular piece of copper; the gas flows through narrow channels (which traverse the copper tube along the axis) that have a radial-spoke cross-section.[29]

A typical mass spectrum is shown in Figure 1, with and without the butylbenzene reactant gas. In the absence of butylbenzene, the O_2^+ signal is dominant (>98%). Common impurities are $H_3O^+(H_2O)_{0,1}$ and $O_2^+(H_2O)$. The ion at 60 amu is $O_2^+(N_2)$. Since the relative concentrations of the impurities were usually less than 2% (sometimes much less), no corrections to the recorded branching ratios were made. When butylbenzene is added, product ions at 43, 78, 91, 92, 105, 119, 134, and 147 amu are observed. The dissociative and nondissociative charge-transfer products at 91/92 and 134 amu, respectively, dominate. In Figure 1, the 91 and 92 amu peaks are merged. This resolution reduces mass discrimination and is used to measure the overall S/D. Higher resolution spectra are used to separate the two peaks, and an isotope correction is made. The mass 43, 78, 105, and 119 amu peaks are present at the same levels as impurities, ca. 0.5−2% at low temperatures. At higher temperatures, the yields of $m/z = 78$, 105, and 119 increase and can be investigated; these originate from the breaking of the various C−C bonds in the side chain; in these cases, the aromatic fragments mainly contain the charge since these are more stable than the alkyl species. The $m/z = 43$ peak of the propyl ion ($C_3H_7^+$), which in Figure 1 is barely detectable (~0.1% of total signal), indicates that as the benzylic C−C bond breaks, see reaction 1.1, less than 1% of the time the charge remains on the alkyl fragment; this conforms with Stevenson's rule: the fragmentation of an ion into two or more channels will favor the formation of the neutral with the highest ionization energy. There is another peak between 55 and 60 amu that could be due to the presence of $C_4H_9^+$ ($m/z = 57$) but here the resolution is too low to differentiate between the butyl ion and impurities. The peak at mass 147 is likely[31] due to a reaction between benzylium and neutral butylbenzene

$$C_7H_7^+(Bz^+) + C_{10}H_{14} \rightarrow C_{11}H_{15}^+ + C_6H_6 \qquad (2.1)$$

Branching ratios of the ion products were recorded as a function of the neutral reagent concentration. Secondary chemistry was taken into account by extrapolating to zero concentration. The accessible temperature and pressure ranges were limited by the allowable intensity of impurity ions (<2%) at low T and high P, and small signals at low P. Fast thermal decomposition and experimental limitations set the upper temperature range.

In the following we consider the reaction scheme

$$O_2^+ + C_{10}H_{14} \rightarrow O_2 + C_{10}H_{14}^{+*} \qquad (2.2a)$$

$$\rightarrow (O_2 - C_{10}H_{14}^+) \rightarrow O_2 + (C_{10}H_{14}^{+*}, C_{10}H_{14}^+) \qquad (2.2b)$$

$$\rightarrow O_2^* + C_{10}H_{14}^+ \qquad (2.2c)$$

$$C_{10}H_{14}^{+*} \rightarrow C_7H_7^+\ (Bz^+, Tr^+) + C_3H_7 \qquad (2.3)$$

$$\rightarrow C_7H_8^+ + C_3H_6 \qquad (2.4)$$

$$C_{10}H_{14}^{+*} + M \rightarrow C_{10}H_{14}^+ + M \qquad (2.5)$$

$$C_{10}H_{14}^+\ (+M) \rightarrow C_7H_7^+ + C_3H_7\ (+M) \qquad (2.6)$$

$$\rightarrow C_7H_8^+ + C_3H_6\ (+M) \qquad (2.7)$$

The three channels in reaction 2.2 represent the three charge transfer mechanisms described in the Introduction. As a reminder, these are resonant charge transfer (2.2a), charge transfer after complex formation (2.2b), and production of electronically excited oxygen, O_2^*, (2.2c). $C_{10}H_{14}^+$ in reactions 2.2b and 2.2c comprises the part of product energy distribution that is nondissociative. The rate coefficient for total production of nondissociating $C_{10}H_{14}^+$ is denoted by $\alpha\ k_2$, whereas $(1 - \alpha)k_2$ corresponds to that fraction of reactions 2.2a and 2.2b which produces $C_{10}H_{14}^{+*}$ with enough energy to dissociate. Reactions 2.2−2.5 characterize chemical activation and reactions 2.6 and 2.7 pyrolysis.

TABLE 1: Stabilization vs Dissociation Yields $S/D = [C_{10}H_{14}^+]/([C_7H_7^+] + [C_7H_8])$ and Pyrolysis Rate Constants k_{pyr}[a]

T/K	P/Torr	S/D	k_{pyr}/s^{-1}
423	15	0.66	
	30	0.72	
	45	0.81	
	60	0.95	
448	65	0.79	
	80	0.81	
	100	1.02	
	150	1.15	
473	15	0.51	
	30	0.59	
	50	0.66	
	75	0.78	
	100	0.87	
498	75	0.46	
	100	0.53	14
	150	0.64	19
	200	0.87	31
	250	0.67	18
523	70	0.47	53
	100	0.70	75
	150	0.67	43
	200	0.90	58
	250	0.74	45
548	70	0.48	
	100	0.42	
	150	0.53	
	200	0.54	
	250	0.59	
423	30 (He)	0.63	
	45 (He)	0.68	

[a] Buffer gas $M = N_2$ except for the last values for $M = He$; S/D values for $T \geq 498$ K correspond to time $t = 0$.

As long as the pyrolysis can be neglected (in our experiments up to temperatures of 473 K), the mass 134 vs (91 + 92) ratio, which we call S/D, can symbolically be written as

$$\frac{S}{D} = \frac{[C_{10}H_{14}^+]}{[C_7H_7^+] + [C_7H_8^+]} \approx \frac{\alpha}{1-\alpha} + \frac{\gamma_c Z[M]}{(1-\alpha)k(E)} \qquad (2.8)$$

For the bath gases M = He and N_2 employed in the present work, the collision frequency Z is approximated by the Langevin rate constant $k_L = 2\pi q(\alpha/\mu)^{1/2}$ with the ionic charge q, the polarizability α of M, and the reduced mass of the collision pair $C_{10}H_{14}^+ + M$. k_L is 5.4×10^{-10} and 6.4×10^{-10} cm^3 molecule^{-1} s^{-1} for M = He and N_2, respectively. $k(E)$ denotes the sum of the specific rate constants of reactions 2.3 and 2.4, i.e., $k_{91}(E) + k_{92}(E)$, at the average energy E reached by processes 2.2a and 2.2b, see below. The collision efficiency γ_c in ref 33 was approximated by a relation involving the properties of the $k(E)$ and the average energy $\langle \Delta E \rangle$ transferred per collision. The details are described below.

On the level of the symbolic relationship 2.8, the intercept of a plot of S/D vs [M] leads to a value of α while the slope corresponds to the ratio $\gamma_c Z/(1 - \alpha)k(E)$. The results of our measurements of S/D as a function of [M] are summarized in Table 1 and illustrated in Figure 2. For temperatures up to 473 K, where no pyrolysis has to be taken into account, the intercept is about 0.5 (±0.1) such that $\alpha \approx 0.33$ (±0.05). However, a more detailed analysis of S/D has to consider the respective energy distributions of the three processes 2.2a, 2.2b, and 2.2c as has been done previously for ethyl and propylbenzene cations in refs 22 and 23. Including the energy distributions causes the intercept to lose its significance. This complete analysis is described in sections 3 and 4.

At temperatures above 498 K, chemical activation and pyrolysis both occur which complicates the analysis. At temperatures $T \leq 473$ K, S/D was found to be independent of the flow tube position at which the $C_{10}H_{14}$ was added indicating that thermal decomposition was not occurring. At higher

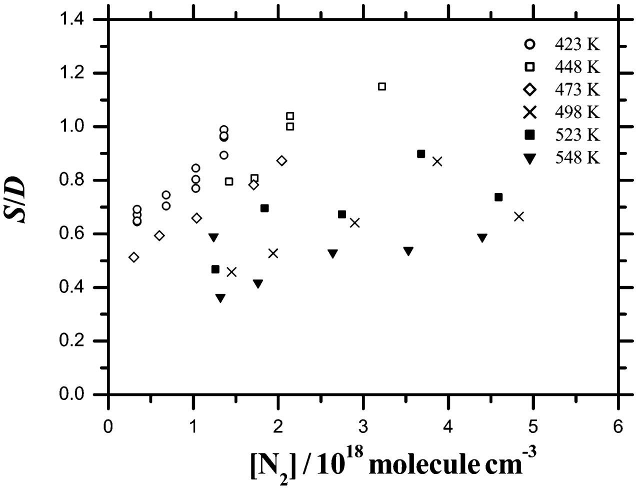

Figure 2. Stabilization (S) vs dissociation (D) yields in chemical activation experiments, with pressures varying between 50 and 250 Torr. At $T \geq 498$ K, pyrolysis is taken into account and the shown S/D is from the extrapolation to time $t = 0$, denoted by $(S/D)_0$; see data given in Table 1.

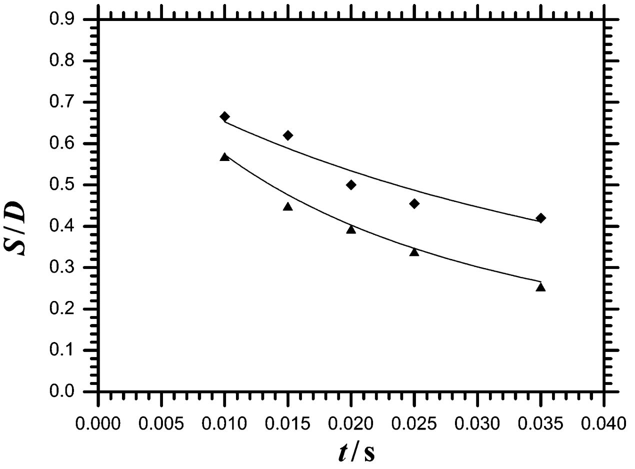

Figure 3. Time dependence of S/D in thermal dissociation experiments. Pressure = 200 Torr; upper curve for 498 K, lower curve for 523 K; full lines = modeling by eq 2.9 with $(S/D)_0 = 0.87$ and $k_{pyr} = 31$ s^{-1} for 498 K, and $(S/D)_0 = 0.90$ and $k_{pyr} = 58$ s^{-1} for 523 K.

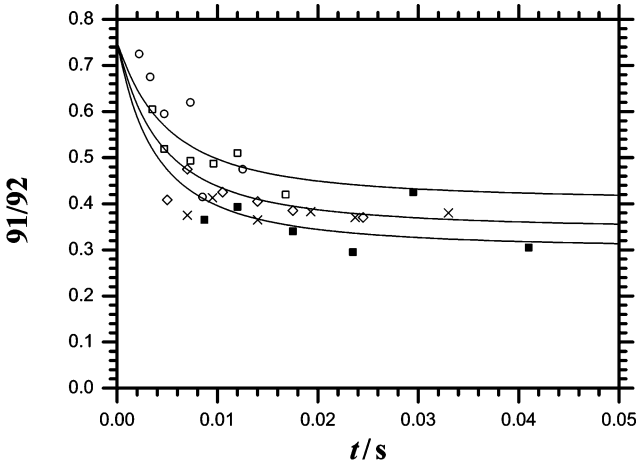

Figure 4. Time dependence of 91/92 in thermal dissociation experiments. $T = 548$ K, pressure/Torr = 70 (○), 100 (□), 150 (◇), 200 (×), and 250 (■); full lines = modeling by eq 2.10 with $(91/92)_0 = 0.75$, $k_{pyr} = 210$ s^{-1}, and $(S/D)_0 = 0.5$ for 70 Torr (upper curve), 0.70 for 150 Torr (middle curve), and 0.88 for 250 Torr (lower curve).

TABLE 2: Minor Fragment Yields $[C_{10}H_{14}^+]/[C_8H_9^+]$ at *m/z* = 105 and Branching Ratio 91/92 = $[C_7H_7^+]/[C_7H_8^+]$[a]

T/K	P/Torr	$[C_{10}H_{14}^+]/[C_8H_9^+]$	$[C_7H_7^+]/[C_7H_8^+]$
423	15	24	
	30	33	
	45	40	
	60	51	
448	70		0.50
	85		0.62
	100		0.61
	110		0.58
	120		0.48
473	15	17	
	30	22	
	50	29	
	75	35	
423	30 (He)	20	
	45 (He)	23	

[a] Buffer gas M = N_2 except for the last two values.

temperatures, S/D decreased when $C_{10}H_{14}$ was added at longer distances, i.e., reaction times. This is a clear indication that thermal dissociation is occurring. This decay can be expressed by the relationship[23]

$$\frac{S}{D} \approx \frac{(S/D)_0\,[1 - \exp(-k_{pyr}t)]}{k_{pyr}t[1 + (S/D)_0] - (S/D)_0\,[1 - \exp(-k_{pyr}t)]} \qquad (2.9)$$

where t denotes the reaction time; the pyrolysis rate constant, k_{pyr}, is given by the sum of the thermal dissociation rate constants of reactions 2.6 and 2.7 and $(S/D)_0$ is the value of S/D at zero reaction time. The $(S/D)_0$ values are listed in Table 1 and shown in Figure 2. Figure 3 shows individual experimental plots of S/D as a function of t for two temperatures. The decays were fit to eq 2.9 by a nonlinear least-squares analysis with $(S/D)_0$ and k_{pyr} as variables and the results shown in Table 1. One should note that the analysis involved both an extrapolation to $[C_{10}H_{14}] = 0$ and a fit to the time dependence, thereby introducing noticeable scatter in the data. The absolute uncertainty of the derived values of k_{pyr} is estimated to be a factor of 1.5; the results are included in Table 1. No pressure dependence of k_{pyr} was observed showing that the high-pressure limit is reached. One also notes that the apparent intercepts of $(S/D)_0$ in Figure 2 decrease with increasing temperature. Our detailed analysis, given in the sections 3 and 4, accounts for this observation. The analysis also suggests that $(S/D)_0$ for 548 K is too low which signals difficulties in separating the chemical from thermal dissociation because the latter dominates.

Table 2 summarizes yields of the most prominent minor fragment (m/z = 105) resulting from reaction 1.4. Ratios of $[C_{10}H_{14}^+]/[C_8H_9^+]$ increase with pressure due to collisional stabilization of an intermediate $C_{10}H_{14}^{+*}$. Although large scatter limited our ability to perform more accurate measurements, we roughly estimate that $k(E)$ for the dissociation of $C_{10}H_{14}^{+*}$ into $C_8H_9^+ + C_2H_5$ is about 2 orders of magnitude smaller than that of the sum of the $k(E)$ for reactions 1.1 and 1.2.

Table 2 also includes measurements of the branching ratio 91/92 = $[C_7H_7^+]/[C_7H_8^+]$ for $T = 448$ K. Within the rather large scatter, a value of about 0.55 was obtained. We could not detect a pressure dependence of 91/92 at that temperature. $[C_7H_7^+]/[C_7H_8^+]$ was also measured as a function of time at higher temperatures during the course of the pyrolysis. Figure 4 shows an example for $T = 548$ K. One can express the change of the branching ratio 91/92 with time as

$$91/92 = (91/92)_0/\{1 + (S/D)_0\,[1 + (91/92)_0][1 - (1 - \exp[-k_{pyr}t])/k_{pyr}t]\} \qquad (2.10)$$

where $(91/92)_0$ is the value of 91/92 at zero reaction time, i.e., in the absence of pyrolysis. At long reaction times, the ratio 91/92 approaches a pressure dependent value of

$$(91/92)_\infty = (91/92)_0/\{1 + (S/D)_0[1 + (91/92)_0]\} \quad (2.11)$$

Figure 4 includes modeled curves employing values for $(91/92)_0$, $(S/D)_0$, and k_{pyr} taken from the modeling described in sections 3 and 4.

Our measurements of the rate constant of the charge exchange reaction 1.3 gave similar results as in the reactions of O_2^+ with ethylbenzene and *n*-propylbenzene. As expected there was no dependence of its rate constant k_3 on the temperature or pressure. An average value of $k_3 = 1.6\ (\pm 0.5) \times 10^{-9}$ cm^3 molecule^{-1} s^{-1} was obtained from our measurements at 423 and 473 K. Using an estimated polarizability of $\alpha = 17.9 \times 10^{-24}$ cm^3 for *n*-$C_{10}H_{14}$,[35,36] the Langevin rate constant for $O_2^+-C_{10}H_{14}$-collisions amounts to 1.95×10^{-9} cm^3 molecule^{-1} s^{-1} which is within the experimental scatter of the measured k_3. Inclusion of the small dipole moment raises this by about 10%.

3. Theoretical Analysis

The analysis of our measured $S/D = [C_{10}H_{14}^+]/([C_7H_7^+] + [C_7H_8^+])$, $91/92 = [C_7H_7^+]/[C_7H_8^+]$, and k_{pyr} is based on specific rate constants $k_{91}(E)$ and $k_{92}(E)$ for the processes 2.3 and 2.4, respectively,[2] on the energy distributions of $C_{10}H_{14}^+$ generated by processes 2.2a, 2.2b, and 2.2c, and[3] on a suitable characterization of the stepwise collisional deactivation process 2.5. Before a detailed modeling of the measured quantities is made, we describe the input parameters used in our approach.

3.1. Specific Rate Constants *k(E,J)*. The specific rate constants $k_{91}(E)$ and $k_{92}(E)$ are taken from the experimental determinations of refs 2 and 3. Their theoretical analysis are given in ref 15 and 17. Process 2.4, corresponding to $k_{92}(E)$ was modeled by RRKM theory in ref 15 using parent ion and activated complex frequencies given in the Appendix. Our own RRKM code confirmed the results from ref 15 which fitted the experimental data over the range $k_{92}(E) = 8 \times 10^4 - 3 \times 10^8$ s^{-1} on the basis of a threshold energy of 1.15 eV (at 0 K). The frequencies were calculated at the B3LYP/6-31G* level and empirically scaled by a factor of 0.9804 for the parent ion, *n*-$C_{10}H_{14}^+$, and by 1.039 for the activated complex frequencies. The necessity to use empirical scaling factors for activated complex frequencies in this type of calculation remains unsatisfactory, but was also observed in our modeling of the isomerization of benzylium to tropylium ions.[16] The various CID models tabulated in ref 15 yielded threshold energies between 1.22 and 1.29 eV. The same work found a value 1.15 eV from a modeling of $k_{92}(E)$. The present measurements of pyrolysis rate constants k_{pyr}, which dominantly correspond to thermal averages over $k_{92}(E)$, confirm the value of 1.15 eV and serves for a test of the various values proposed previously.

Unlike process 2.4, the simple bond fission (2.3) to produce benzylium cannot be accurately modeled by rigid activated complex RRKM theory over large energy ranges. The SACM/CT calculations presented in ref 17 have overcome this problem. In that study, the threshold energy for (2.3) was fit to 1.78 eV. This is in contrast to the RRKM fit[15] of 1.57 eV. The various CID models tabulated in ref 15 led to values in the range 1.70−1.96 eV. The SACM/CT treatment also provides information on the *J* dependence of $k_{91}(E)$ which is required for an adequate determination of the corresponding pyrolysis rate constant, see ref 17. In the present modeling of the chemical activation process, we neglected the *J* dependence, whereas the modeling of the thermal dissociation rate constants included this dependence (see ref 17 for the modeling of the reverse recombination of $C_7H_7^+$ with C_3H_7).

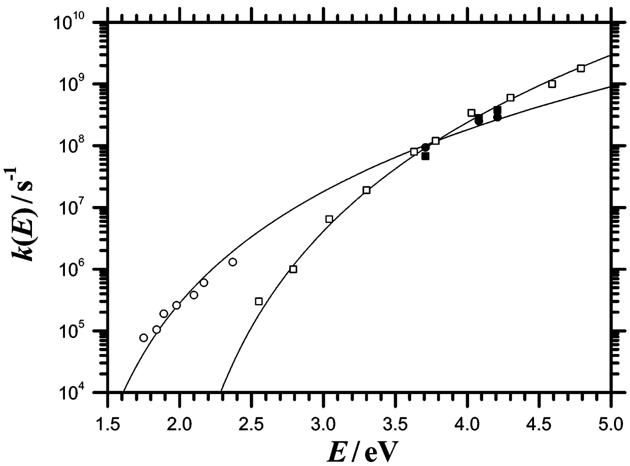

Figure 5. Empirical representation of the specific rate constants $k_{91}(E)$ and $k_{92}(E)$ by eqs 3.1 and 3.2. Open symbols: experiments from ref 2; closed symbols: experiments from ref 3; squares: $k_{91}(E)$; circles: $k_{92}(E)$; full lines: eqs 3.1 and 3.2.

The specific rate constants $k_{91}(E)$ and $k_{92}(E)$ described above can conveniently be expressed by simple analytical expressions. We employ

$$k_{91}(E) \approx 2.6 \times 10^7\ s^{-1}\ \{[E - E_0(91)]/[E_{ch} - E_0(91)]\}^{s^*_{91}-1} \quad (3.1)$$

$$k_{92}(E) \approx 4.9 \times 10^7\ s^{-1}\ \{[E - E_0(92)]/[E_{ch} - E_0(92)]\}^{s^*_{92}-1} \quad (3.2)$$

with the energy E_{ch} reached by charge exchange (at 0 K) given as $E_{ch}/hc = 27\,260$ cm^{-1}, $E_0(91)/hc = 14\,360$ cm^{-1}, $E_0(92)/hc = 9275$ cm^{-1}, $s^*_{91} = 7.77$, and $s^*_{92} = 6.34$ (see the Appendix for the energy parameters employed). Figure 5 compares eqs 3.1 and 3.2 to the experimental data. One realizes that the experimental data between 10^5 and 10^9 s^{-1} are well reproduced. Disagreements with RRKM and SACM/CT modeling become important only below 10^3 s^{-1}, especially for $k_{91}(E)$, see ref 17. These discrepancies are irrelevant for the chemical activation experiments while they matter when modeling the pyrolysis rate constants or determining the bond energy.

A modeling of *S*/*D* only requires a representation of the sum $k(E) = k_{91}(E) + k_{92}(E)$. Combining eqs 3.1 and 3.2 over the energy range relevant in our chemical activation experiments leads to

$$k(E) \approx 7.6 \times 10^7\ s^{-1}\ \{[E - E_0(92)]/[E_{ch} - E_0(92)]\}^{s^*-1} \quad (3.3)$$

with $s^* = 8.0$. Equation 3.3 was used for determining γ_c, whereas eqs 3.1 and 3.2 were used otherwise.

3.2. Energy Distributions from Charge Transfer. Our characterization of the energy distributions from the three charge-transfer mechanisms in reaction 2.2 follows the method described in ref 22. We assume that resonant charge transfer (2.2a) maps the thermal energy distribution of *n*-$C_{10}H_{14}$ into that of *n*-$C_{10}H_{14}^+$ on top of the difference of the ionization energies of O_2 and *n*-$C_{10}H_{14}$. Figure 6 shows an example of the corresponding energy distribution. The vibrational frequencies of *n*-$C_{10}H_{14}$ and the relevant energy parameters employed in

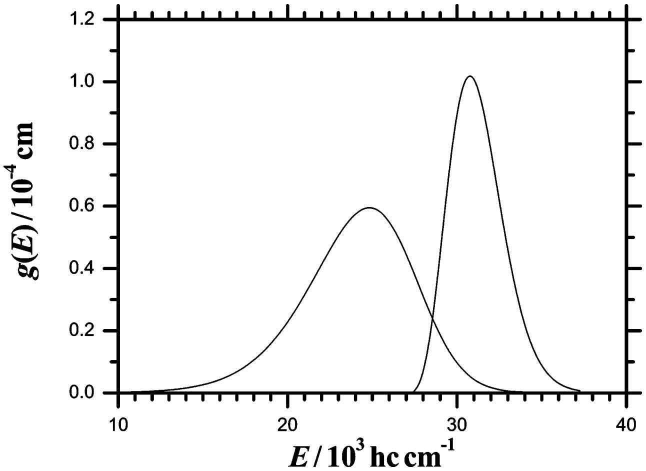

Figure 6. Typical energy distributions from resonant (curve at right) and complex-forming charge transfer (curve left). Modeling for $\langle E_{th}(423\ K)\rangle/hc = 3680\ cm^{-1}$; the assumed branching ratios for channels 2.2a, 2.2b, and 2.2c are $g_a = 0.4$, $g_b = 0.47$, and $g_c = 0.13$, respectively.

the calculation are included in the Appendix. The energy distribution of charge-transfer involving intermediate complex formation, reaction 2.2b, analogous to the $O_2^+ + C_8H_{10}$ reaction treated in ref 22 can satisfactorily be represented by an expression

$$P(E,E_B) \approx A'(E - E_B)^5 \exp[-5(E - E_B)/(E - E_B)_{max}] \tag{3.4}$$

where $E \approx E_{ch} + E_{th}$, E_{th} is the thermal vibrational energy of $C_{10}H_{14}$, E_B is the vibrational energy of $C_{10}H_{14}^+$, and $(E - E_B)_{max}$ denotes the maximum of the distribution. One should note that the distribution 3.4 has to be convoluted with the thermal distribution of n-$C_{10}H_{14}$. Figure 6 shows the distribution for $E = \langle E_{th}(423\ K)\rangle$. A′ is the normalization factor obtained from the condition $\int_0^E P(E - E_B)\, dE_B = 1$. Our modeling gave $(E - E_B)_{max}/hc \approx 6000\ cm^{-1}$, close to the corresponding value of 5500 cm^{-1} for $C_8H_{10}^+$ found in ref 22.

The third channel 2.2c, producing electronically excited $O_2(^1\Delta_g)$ at hc 7882 cm^{-1} or $O_2(^1\Sigma_g^+)$ at hc 13121 cm^{-1} only needs to be characterized by its relative contribution since it leads to nondissociative $C_{10}H_{14}^+$. As we do not have sufficiently reliable S/D measurements at very low pressures, we use the same charge-transfer branching ratio for channel 2.2c as found in refs 22 and 23, e.g., $g_c \approx 0.13$. We then fit g_a (for resonant charge transfer 2.2a) by comparison with measured S/D values or branching ratios 91/92. This then fixes $g_b = 1 - g_a - g_c$ (for complex-forming charge transfer 2.2b). The measured S/D values as a function of pressure are not sufficiently accurate and do not extend over a sufficiently large pressure range to be able to accurately fit the charge-transfer branching ratios and the energy transfer parameter $\langle \Delta E\rangle$ independently. However, measurements of the branching ratio 91/92 again provide a molecular thermometer and allow for a distinction between various values of g_a and g_b after g_c is fixed to the same value used in the analysis of our $C_8H_{10}^+$ experiments ($g_c \approx 0.13$). In practice, both the S/D curves and the value of 91/92 were used to optimize an estimate of g_a.

3.3. Collisional Energy Transfer Model. Our previous investigations of the collisional stabilization of chemically activated $C_8H_{10}^+$ and $C_9H_{12}^+$ ions employed a simplified collision model based on a stepladder mechanism (down-steps only). The critical parameter needed in eq 2.8 is the collision efficiency γ_c. Following the treatment from ref 33 (see also ref 34), γ_c in the high-pressure range of the stepladder model can be calculated from the approximate relationship

$$\frac{\gamma_c}{1 - \gamma_c^{\ 2}} \approx \frac{-\langle \Delta E\rangle\, s^*}{E - E_0} \tag{3.5}$$

if $S/(S + D)$ is expressed by

$$S/(S + D) \approx \gamma_c Z\,[M]/\{\gamma_c Z\,[M] + k_{91}(E) + k_{92}(E)\} \tag{3.6}$$

s^* and E_0 in eq 3.5 can be taken from eq 3.3. After averaging $S/(S + D)$ over the energy distribution from section 3.2, $\langle \Delta E\rangle$ can be obtained from the measured S/D.

Equations 5 and 3.6 in ref 33 have been obtained from the “stochastic” model for collisional stabilization which expresses $S/(S + D)$ by

$$\frac{S}{S + D} = \prod_{i=1}^{T} \frac{Z[M]}{Z[M] + k(E_i)} \tag{3.7}$$

Here T denotes the number of steps of size $|\langle \Delta E\rangle|$ required to stabilize the activated molecule starting at an energy E_{ac}. Approximating this by $T \approx (E_{ac} - E_0)/|\langle \Delta E\rangle|$ and focusing attention on the high-pressure range $k(E_i) \ll Z[M]$, eq 3.7 leads to $\gamma_c \approx k(E_{ac})/\sum_{i=1}^{T} k(E_i)$ (as long as $T \gg 1$). Replacing the Σ by an integral finally leads to

$$\gamma_c \approx \frac{|\langle \Delta E\rangle| s^*}{E_{ac} - E_0} \tag{3.8}$$

When γ_c approaches unity, the denominator $1 - \gamma_c^2$ needs to be added at the left-hand side of eq 3.8, see ref 33; in the present case, γ_c is of the order of 0.1 such that eq 3.8 is adequate.

The present two-channel character of the reaction provides the opportunity to exploit measurements of the branching ratio 91/92. At each step of the collisional deactivation sequence, there is the competition between reactions 2.3 and 2.4. In the high-pressure range of the reaction, $S/(S + D)$ at each step remains close to unity and the populations are only depleted by reaction to a small extent. At the same level of approximation as eqs 3.5 and 3.6, one then may express $D_i/(S + D)$ by

$$\frac{D_i}{S + D} \approx \frac{k_i(E_{ac})}{\gamma_{ci} Z[M] + \sum_i k_i(E_{ac})} \approx \frac{k_i(E_{ac})}{\gamma_{ci} Z[M]} \tag{3.9}$$

where i stands for the channels 91 and 92 and γ_{ci} denotes the corresponding collision efficiencies. To a first approximation the branching ratio 91/92 then is given by

$$\frac{91}{92} \approx \frac{k_{91}(E_{ac})[E_{ac} - E_0(91)]s_{92}^*}{k_{92}(E_{ac})[E_{ac} - E_0(92)]s_{91}^*} \tag{3.10}$$

We have compared eq 3.10 with results from a detailed master equation model for exponential collisions. Analogous to the results for single channel dissociation in ref 33, only small deviations from eq 3.10 were found. Therefore, eq 3.10 appears adequate for the present analysis of the experimental data after convolution with the energy distributions. Equations 3.1 and 3.2 provide the required input data to eq 3.10.

3.4. Thermal Dissociation Rate Constants. The pyrolysis rate constants k_{pyr} measured in the TIFT correspond to the high-pressure limit of the unimolecular reactions 2.7 and 2.8, denoted by $k_{\mathrm{diss},\infty}(91)$ and $k_{\mathrm{diss},\infty}(92)$, respectively. They are given by

$$k_{\mathrm{diss},\infty}(i) = \sum_{J=0}^{\infty} (2J+1) \int_{E_{0i}(J)}^{\infty} k_i(E, J)\, f(E, J, T)\, \mathrm{d}E \quad (3.11)$$

It will be shown that under our conditions k_{pyr} is dominated by $k_{\mathrm{diss},\infty}(92)$ which is expressed by rigid activated complex transition state theory,

$$k_{\mathrm{diss},\infty}(92) = \frac{\mathrm{k}T}{\mathrm{h}} \frac{Q_{\mathrm{rot}}^{\neq}}{Q_{\mathrm{rot}}} \frac{Q_{\mathrm{vib}}^{\neq}}{Q_{\mathrm{vib}}} \exp\left(-\frac{E_0(92)}{\mathrm{k}T}\right) \quad (3.12)$$

The frequencies used to calculate Q_{vib} and $Q_{\mathrm{vib}}^{\neq}$ are given in the Appendix. They are consistent with the measured $k_{92}(E)$. The rotational constants required for $Q_{\mathrm{rot}}^{\neq}$ and Q_{rot} are taken from the B3LYP/6-31G* calculations reported in ref 15 and listed in the Appendix.

To predict at which temperatures $k_{\mathrm{diss},\infty}(91)$ may also play a role, we have determined this value from the SACM/CT modeling of $k_{91}(E,J)$ described in refs 17 and 37. Here $k_{\mathrm{rec},\infty}(91) = K_c(91)\, k_{\mathrm{diss},\infty}(91)$ was calculated in a manner consistent with the measured $k_{91}(E)$. The equilibrium constant $K_c(91)$ was calculated with the data given in the Appendix. It appears worth noting that $k_{\mathrm{rec},\infty}(91)$ and $k_{91}(E)$ are more than 2 orders of magnitude smaller than the corresponding values from phase space theory. The results are documented in section 4.

4. Modeling Results

In this section. we analyze our experimental results within the framework of the modeling described in section 3. The measurements of k_{pyr} are interpreted first, as they provide an accurate determination of $E_0^{(92)}$. Then, the measured branching ratios, 91/92, are used as molecular thermometers to provide information on the relative contributions of the three charge-transfer mechanisms. Finally, the measured S/D curves as a function of pressure and temperature are simulated using this information and $\langle \Delta E \rangle$ determined by fitting.

4.1. Thermal Dissociation Rate Constants. The ratio $Q_{\mathrm{vib}}^{\neq}/Q_{\mathrm{vib}}$ needed in eq 3.12 for the channel forming $C_7H_8^+$ can be established without much uncertainty using the activated complex frequencies calibrated empirically[15] to the experimental $k_{92}(E)$. The ratio $Q_{\mathrm{rot}}^{\neq}/Q_{\mathrm{rot}}$ from the B3LYP/6-31G* calculations[15] only have a small uncertainty. The preexponential factor of $k_{\mathrm{diss},\infty}(92)$, therefore, should be reliable enough to allow for a fit of $E_0^{(92)}$ from the experimental values of k_{pyr} (under the condition that $k_{\mathrm{diss},\infty}(91)$ can be neglected). Combining the measured values of k_{pyr} of 21 and 55 s^{-1} for $T = 498$ and 523 K, respectively and the calculated preexponential factors 1.04×10^{14} and 1.09×10^{14} s^{-1} leads to of $E_0(92)$ values of 1.145 and 1.14 eV, respectively. From these data, we obtain

$$E_0(92) = 1.14\ (\pm 0.02)\ \mathrm{eV} \quad (4.1)$$

in excellent agreement with the value 1.15 (±0.1) eV from the RRKM analysis of $k_{92}(E)$ provided in ref 15. The present value has a much smaller error that is estimated from the uncertainty in the absolute value of k_{pyr}. The values derived from CID measurements in ref 15 are all (up to 0.15 eV) higher. The CID values of E_0 would be consistent with our measurements only if k_{pyr} would be a factor of 30 smaller than observed in our work, well outside our estimated error. Therefore, the higher values of $E_0(92)$ clearly can be ruled out.

The thermal dissociation rate constant $k_{\mathrm{diss},\infty}(91)$ is markedly smaller than $k_{\mathrm{diss},\infty}(92)$. The properties of $k_{\mathrm{diss},\infty}(91)$ can be predicted on the basis of the experimental $k_{91}(E)$. Although the experimental $k_{91}(E)$ can well be represented by eq 3.1 as shown in Figure 5, the SACM/CT study of ref 17 provided a complete set of $k_{91}(E,J)$ as well as of $E_0(J)$ consistent with the experiments. It also gave values of k_{91}^{PST} in the framework of phase space theory (PST) which neglects the anisotropy of the potential. The modeling results from ref 17 could be expressed by

$$k_{91}(E,J)/k_{91}^{\mathrm{PST}}(E,J) = f_{\mathrm{rigid}}(E,J) \approx c_1 + (1 - c_1)\exp\{-[E - E_0(J)]/c_2\} \quad (4.2)$$

with $c_1 = 0.0037$, $c_2/\mathrm{hc} = 125\ \mathrm{cm}^{-1}$, and

$$E_0(J)/\mathrm{hc} \approx 2.47 \times 10^{-7}\ \mathrm{cm}^{-1}\ J^4(1 + 1.81 \times 10^{-2}\ J^{0.879} + 3.67 \times 10^{-4}\ J^{1.601}) \quad (4.3)$$

$E_0(J)$ in eq 4.3 is counted relative to the separated fragments. Equation 4.3 directly leads to the capture PST rate constants for recombination of $C_7H_7^+ + C_3H_7$

$$k_{\mathrm{cap}}^{\mathrm{PST}}(91) = \frac{\mathrm{k}T}{\mathrm{h}} \left(\frac{\mathrm{h}^2}{2\pi\mu \mathrm{k}T}\right)^{3/2} \sum_{J=0}^{\infty} (2J+1) \exp[-E_0(J)/\mathrm{k}T] \quad (4.4)$$

Numerical evaluation of eqs 4.2 and 4.4 leads to[37] $k_{\mathrm{cap}}^{\mathrm{PST}}(91) = 1.1\ (\pm 0.1) \times 10^{-9}\ \mathrm{cm}^3\ \mathrm{molecule}^{-1}\ \mathrm{s}^{-1}$ and $f_{\mathrm{rigid}} = 0.018$ (±0.003) over the range 498−548 K. The equilibrium constant $K_c(91)$ over the range 400−800 K is represented by

$$K_c(91) \approx 1.6 \times 10^{-27}\ (T/498\ \mathrm{K})^{+0.5} \exp(+E_0(91)/\mathrm{k}T)\ \mathrm{cm}^3\ \mathrm{molecule}^{-1} \quad (4.5)$$

with $E_0(91) = 1.78$ eV. More precisely, we predict $k_{\mathrm{diss},\infty}(91) = k_{\mathrm{cap}}(91)/K_c(91)$ to be equal to 0.015, 0.089, and 0.46 s^{-1} for $T = 498$, 523, and 548 K, respectively. Comparing these to the overall pyrolysis rates shows that under the present conditions the dissociation forming $C_7H_8^+ + C_3H_6$ is approximately 10^3 times faster than for the $C_7H_7^+ + C_3H_7$ channel.

Extending our modeling to temperatures outside the range of our experiments, between 400 and 800 K gives

$$k_{\mathrm{diss},\infty}(91) \approx 1.5 \times 10^{14} \exp(-18\,590\ \mathrm{K}/T)\ \mathrm{s}^{-1} \quad (4.6)$$

and

$$k_{\mathrm{diss},\infty}(92) \approx 1.0 \times 10^{13} \exp(-13\,480\ \mathrm{K}/T)\ \mathrm{s}^{-1} \quad (4.7)$$

On this basis, we conclude that the rate of reaction 2.6 exceeds that of reaction 2.7 at $T > 2000$ K. In a combustion situation, both processes may occur. It appears worth noting that the positive temperature coefficient of the preexponential factor of K_c and the negative temperature coefficient of f_{rigid} lead to a comparably small preexponential factor and apparent activation energy of $k_{\mathrm{diss},\infty}(91)$ (for which $E_0^{(91)}/\mathrm{k}$ would be equal to 20 660 K).

4.2. Branching Ratios 91/92. Equation 3.10 may serve as our molecular thermometer for an estimate of the relative contributions of the charge-transfer components 2.2a and 2.2b, such as described in section 3.3. In the following, we illustrate the sensitivity of the ratio 91/92 on the contributions from resonant (reaction 2a, branching ratio g_a) and complex-forming charge transfer (reaction 2b, branching ratio g_b). Leaving g_c unchanged at 0.13 and considering the temperature $T = 448$ K,

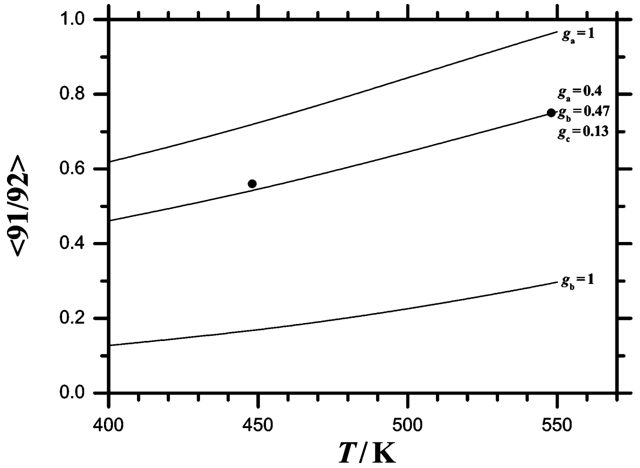

Figure 7. Effective branching ratios 91/92 for chemical activation experiments as a function of temperature. Lower curve = modeling results for $g_a = 0$, $g_b = 1$, and $g_c = 0$, i.e., completely complex-forming charge transfer; middle curve = modeling results for $g_a = 0.4$, $g_b = 0.47$, and $g_c = 0.13$; upper curve = modeling results for $g_a = 1$, $g_b = 0$, and $g_c = 0$, i.e., completely resonant charge transfer.

one has average energies of 3.736 eV at $g_a = 0.6$ and 3.586 eV at $g_a = 0.4$. Using these energies for E_{ac} in eq 3.10, one would have 91/92 = 0.58 in the former and 91/92 = 0.46 in the latter case. The case $g_a = 1$, corresponding to exclusively resonant charge transfer, would lead to an average energy of 3.872 eV and 91/92 = 0.71. In reality, the energy dependent branching ratio 91/92 from eq 3.10 needs to be averaged over the energy distribution generated by charge transfer. Doing this, for $T = 448$ K (and leaving $g_c \approx 0.13$ unchanged), we obtain 91/92 = 0.63 and 0.54 for $g_a = 0.6$ and 0.4, respectively. As the experimental value of 0.55 is close to the latter case, we employ $g_a = 0.4$, $g_b = 0.47$, and $g_c = 0.13$ for our modeling of the S/D curves. The assumption of completely resonant charge transfer ($g_a = 1$) with an average 91/92 = 0.72 apparently is ruled out by our measurements. This is also confirmed by our measurements of S/D discussed below. Figure 7 shows the effective branching ratios of our experiments as a function of temperature, comparing modeling results for (g_a, g_b, g_c) = (0.4, 0.47, 0.13) with results for $g_a = 1$, i.e., completely resonant charge transfer, and $g_b = 1$, i.e., completely complex-forming charge transfer. Neither $g_a = 1$ nor $g_b = 1$ are compatible with the measured 91/92 = 0.55 at 448 K given above and $(91/91)_0 = 0.75$ at 548 K such as extrapolated to time zero in Figure 4.

4.3. Stabilization vs Dissociation. Our modeling of the experimental S/D curves as a function of buffer gas, pressure, and temperature follows the procedure described in ref 22 and in section 3.3. The averaging over the distribution $g(E,T)$ from the charge-transfer components 2.2a−2.2c is done with the branching ratios $g_a = 0.4$, $g_b = 0.47$, and $g_c = 0.13$, such as suggested in section 4.2, and the averaging over the energy distributions described in section 3.2. S/D then is given by[22]

$$S/D = Z[\mathrm{M}] \int_0^\infty \mathrm{d}E\, g(E,T)\gamma_c(E)/[k_{91}(E) + k_{92}(E)] \quad (4.8)$$

with $\gamma_c(E)$ from eq 3.5 using $E_0 = E_0(92)$ and $s^* \approx 8.0$, and $k_{91}(E) + k_{92}(E)$ from eqs 3.1 and 3.2. The results are shown in Figure 8 where the experimental points from Figure 2 are compared with the modeling results from eq 4.8.

The modeling in Figure 8 has been done employing the average energy transferred per collision $-\langle \Delta E \rangle/hc = 285$ cm^{-1} for M = N$_2$. This is value found for the $C_8H_{10}^+$ system in ref 22. Performing analogous modeling for the limited experimental data for M = He given in Table 1 yields a similar result, $-\langle \Delta E \rangle/hc = 180$ cm^{-1}, to that found for $C_8H_{10}^+$ in ref 22. One notes that the experimental S/D curves and their temperature dependence can be reproduced within the experimental scatter. One should note that we have evaluated the curve at the highest temperature (548 K), by fixing k_{pyr} at 210 s^{-1} such as given by eq 4.7. At this temperature, the thermal dissociation becomes too fast to allow for a separate determination of k_{pyr} and $(S/D)_0$. The agreement of the modeled and measured S/D curves in Figure 8 is by no means perfect. First, there is considerable experimental scatter. Second, we have assumed that the charge-transfer branching ratios g_a, g_b, and g_c are temperature independent. Small temperature dependences of g_a would improve the agreement. We have not employed such corrections since we have too little conclusive evidence for this behavior and g_c remains uncertain. Nevertheless, our results support the conclusion that collisional energy transfer of vibrationally highly excited molecular ions is not very much more efficient with respect to $\langle \Delta E \rangle$ than the corresponding transfer in neutrals. However, somewhat larger values of $|\langle \Delta E \rangle|$ seem to be observed. On the other hand, the collision frequencies Z for ions are much larger (given by the Langevin rate constant in the present case) than for neutrals (mostly given by Lennard-Jones collision numbers), resulting in an overall rate that is larger than for neutral systems.

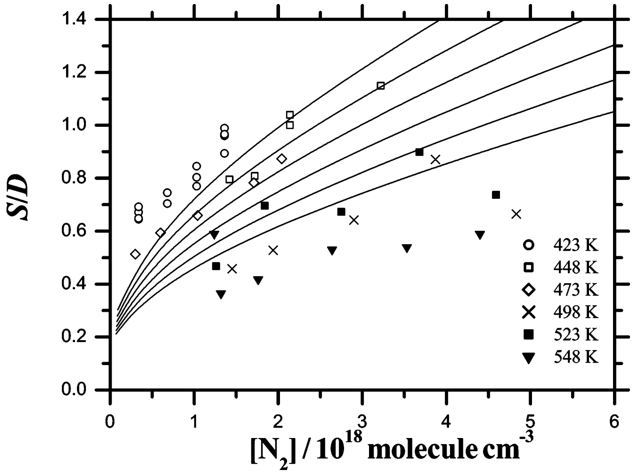

Figure 8. Stabilization (S) vs dissociation (D) yields in chemical activation experiments. Data from Figure 2 modeled with $g_a = 0.4$, $g_b = 0.47$, $g_c = 0.13$, and $-\langle \Delta E \rangle/hc = 285$ cm^{-1}, see text.

The present modeling also allows for a prediction of S/D over larger pressure ranges such as this has been demonstrated for the $C_8H_{10}^+$ system in ref 22. Figure 9 shows a plot of S/D over much wider pressure ranges than studied here.

One may also employ the S/D curves to investigate the relevance of the three components of the charge-transfer processes 2.2a−2.2c as has been done above using the branching ratio of 91/92. Figure 10 demonstrates that purely resonant charge transfer ($g_a = 1$) is unable to reproduce the data, particularly at low pressures, even if very large values of $|-\langle \Delta E \rangle|$ corresponding to $\gamma_c = 1$ are employed. Likewise, purely complex-forming charge transfer is unable to account for the observed S/D and 91/92. The combination of both S/D and 91/92 measurements in the present work, therefore, supports the conclusion from ref 22 that charge transfer between O_2^+ and alkylbenzenes is characterized by several components such as symbolized by reactions 2.2a, 2.2b, and 2.2c. Channels 2.2a and 2.2b apparently contribute in about equal amounts.

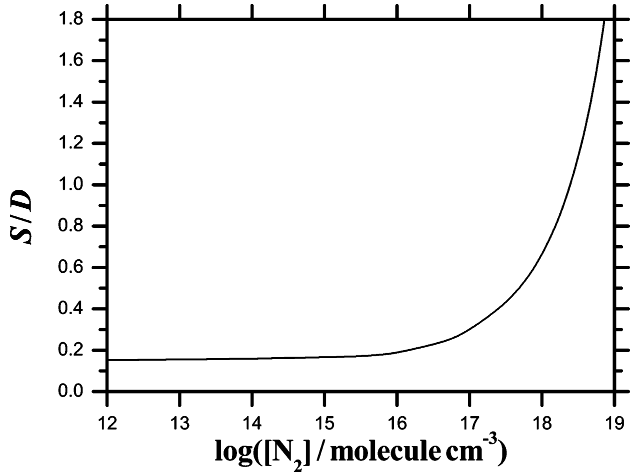

Figure 9. Modeled *S*/*D* over wide pressure ranges ($T = 448$ K, M = N_2, modeling details as in Figure 8).

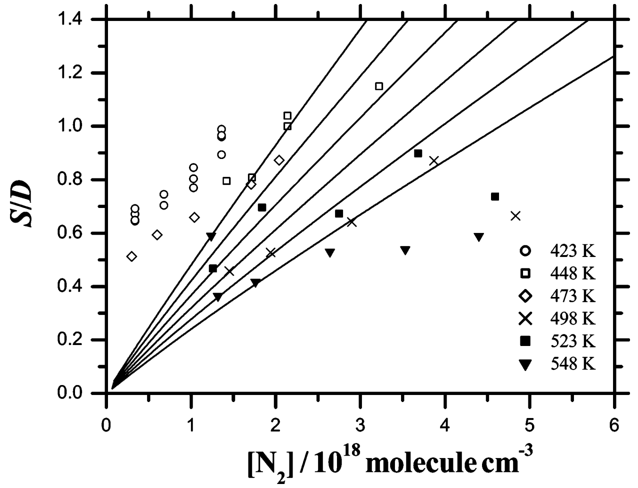

Figure 10. As in Figures 2 and 8 with a modeling assuming completely resonant charge transfer ($g_a = 1$, see text) and strong collisions ($-\langle\Delta E\rangle/hc = 5000$ cm^{-1}).

5. Conclusions

Our measurements of the combined chemical and thermal activation kinetics of vibrationally highly excited *n*-butylbenzene cations, reacting to form two competing channels, have been analyzed in detail. The branching ratio 91/92 served as a "molecular thermometer" such as demonstrated in earlier studies of this system. In the present case, it provided information on the relative contributions from resonant and complex-forming charge transfer between O_2^+ and *n*-butylbenzene. *S*/*D* curves in the chemical activation experiments could be reproduced within the experimental scatter from information on specific rate constants *k*(*E*) for the dissociation of $C_{10}H_{14}^{+*}$ and on collisional energy transfer. Completely resonant charge transfer or charge transfer through a complex between O_2^+ and n-$C_{10}H_{14}$ is not compatible with either the 91/92 branching or the *S*/*D* curves. The thermal dissociation experiments provide a high precision value for the energy barrier of the reaction leading to the fragments $C_7H_8^+ + C_3H_6$ which is consistent with *k*(*E*) measurements of this channel. Our work demonstrates again that the *n*-butylbenzene cation is a particularly suitable system for studying two-channel competition in the dissociation of molecular cations.

Acknowledgment. This project was funded by the United States Air Force Office of Scientific Research under Project 2303EP4 and Grant Award FA8655-03-1-3034. Financial support by the Deutsche Forschungsgemeinschaft (SFB 357 "Molekulare Mechanismen unimolekularer Reaktionen") as well as help by A. I. Maergoiz are also gratefully acknowledged.

6. Appendix: Molecular Parameters

1. Frequencies (in cm^{-1}): n-$C_{10}H_{14}$: 3144, 3131, 3123, 3109, 3108, 3054, 3047, 3027, 3003, 3001, 2984, 2979, 2968, 2967, 1633, 1611, 1516, 1509, 1502, 1500, 1489, 1481, 1472, 1413, 1373, 1368, 1344, 1335, 1320, 1297, 1269, 1210, 1204, 1189, 1168, 1116, 1103, 1068, 1056, 1038, 998, 973, 961, 945, 933, 907, 867, 843, 814, 782, 748, 733, 702, 624, 587, 500, 411, 408, 333, 286, 270, 207, 120, 92, 45, 24 (B3LYP/6-31G* calculations from this work with scaling factor 0.9804).

n-$C_{10}H_{14}^+$: 3177, 3173, 3162, 3156, 3155, 3082, 3072, 3061, 3058, 3031, 3022, 3010, 2995, 2993, 1639, 1517, 1505, 1497, 1487, 1484, 1476, 1459, 1397, 1395, 1382, 1336, 1328, 1285, 1280, 1252, 1236, 1226, 1202, 1196, 1160, 1092, 1053, 1051, 1004, 995, 986, 986, 982, 976, 948, 879, 847, 805, 789, 777, 767, 732, 627, 541, 527, 435, 364, 361, 343, 244, 234, 179, 119, 69, 64, 40 (B2LYP/6-31G* calculations from ref 15 with scaling factor 0.9804).

Transition state for $C_{10}H_{14}^+ \rightarrow C_7H_8^+ + C_3H_6$: 3395, 3382, 3359, 3347, 3328, 3301, 3293, 3284, 3264, 3196, 3151, 3129, 3076, 1710, 1663, 1614, 1601, 1573, 1562, 1548, 1509, 1504, 1481, 1471, 1465, 1411, 1362, 1351, 1267, 1253, 1252, 1243, 1124, 1110, 1086, 1064, 1059, 1047, 1040, 1030, 1006, 986, 970, 960, 956, 895, 853, 810, 756, 746, 619, 549, 520, 477, 442, 377, 310, 257, 178, 157, 125, 81, 67, 39 (B3LYP/6-31G* calculations from ref 15 with empirical scaling factor of 1.039 chosen to match *k(E)* measurements for reaction 1.2).

2. Rotational constants (in cm^{-1}): n-$C_{10}H_{14}^+$: $A_e = 0.116$, $B_e = 0.019$; $C_7H_7^+$: $A_e = 0.178$, $B_e = 0.075$; n-C_3H_7: $A_e = 1.044$, $B_e = 0.278$; TS:^{92} $A_e = 0.089$, $B_e = 0.021$ from ref 15.

3. Energy parameters: IE(O_2) = 12.07 eV, IE(n-$C_{10}H_{14}$) = 8.69 eV from ref 38 leading to $E_{ch}/hc = 27260$ cm^{-1}. $E_0^{91} = 1.78$ ($\pm$0.05) eV from ref 17, $E_0^{92} = 1.15$ ($\pm$0.1) eV from ref 15, 1.14 ($\pm$0.02) eV from this work.

References and Notes

(1) Baer, T.; Hase, W. L. *Unimolecular Reaction Dynamics. Theory and Experiments*; Oxford University Press: Oxford, 1996.

(2) Baer, T.; Dutuit, O.; Mestdagh, H.; Rolando, C. *J. Phys. Chem.* **1988**, *92*, 5674.

(3) Oh, S. T.; Choe, J. C.; Kim, M. S. *J. Phys. Chem.* **1996**, *100*, 13367.

(4) Mukhtar, E. S.; Griffith, I. W.; Harris, F. M.; Beynon, J. H. *Int. J. Mass Spectrom. Ion Phys.* **1981**, *37*, 159.

(5) Griffith, I. W.; Mukhtar, E. S.; March, R. E.; Harris, F. M.; Beynon, J. H. *Int. J. Mass Spectrom. Ion Phys.* **1981**, *39*, 125.

(6) Griffith, I. W.; Mukhtar, E. S.; Harris, F. M.; Beynon, J. H. *Int. J. Mass Spectrom. Ion Phys.* **1982**, *43*, 283.

(7) McLuckey, S. A.; Sallans, L.; Cody, R. G.; Burnier, R. C.; Verma, S.; Freiser, B. S.; Cooks, R. G. *Int. J. Mass Spectrom. Ion Phys.* **1982**, *44*, 215.

(8) McLuckey, S. A.; Ouwerkerk, C. E. D.; Boerboom, A. J. H.; Kistemaker, P. *Int. J. Mass Spectrom. Ion Processes* **1984**, *59*, 85.

(9) Harrison, A. G.; Lin, M. S. *Int. J. Mass Spectrom. Ion Phys.* **1983**, *51*, 353.

(10) Chen, J. H.; Hays, J. D.; Dunbar, R. C. *J. Phys. Chem.* **1984**, *88*, 4759.

(11) Welch, M. J.; Pereles, D. J.; White, E. *Org. Mass Spectrom.* **1985**, *20*, 425.

(12) Nacson, S.; Harrison, A. G. *Int. J. Mass Spectrom. Ion Processes* **1985**, *63*, 85.

(13) Uechi, G. T.; Dunbar, R. C. *J. Chem. Phys.* **1992**, *96*, 8897.

(14) Yoon, O. K.; Hwang, W. G.; Choe, J. C.; Kim, M. S. *Rapid Commun. Mass Spectrom.* **1999**, *13*, 1515.

(15) Muntean, F.; Armentrout, P. B. *J. Phys. Chem. A* **2003**, *107*, 7413.

(16) Fridgen, T. D.; McMahon, T. B.; Troe, J.; Viggiano, A. A.; Midey, A. J.; Williams, S. *J. Phys. Chem. A* **2004**, *108*, 5600.

(17) Troe, J.; Ushakov, V. G.; Viggiano, A. A. *J. Phys. Chem. A* **2006**, *110*, 1491.

(18) Viggiano, A. A.; Miller, T. M.; Williams, S.; Arnold, S. T.; Seeley, J. V.; Friedman, J. F. *J. Phys. Chem. A* **2002**, *106*, 11917.

(19) Arnold, S. T.; Seeley, J. V.; Williamson, J. S.; Mundis, P. L.; Viggiano, A. A. *J. Phys. Chem. A* **2000**, *104*, 5511.

(20) Arnold, S. T.; Viggiano, A. A. *J. Phys. Chem. A* **2001**, *105*, 3527.

(21) Midey, A. J.; Williams, S.; Arnold, S. T.; Viggiano, A. A. *J. Phys. Chem. A* **2002**, *106*, 11726.

(22) Troe, J.; Viggiano, A. A.; Williams, S. J. *J. Phys. Chem. A* **2004**, *108*, 1574.

(23) Fernandez, A. I.; Viggiano, A. A.; Miller, T. M.; Williams, S.; Dotan, I.; Seeley, J. V.; Troe, J. *J. Phys. Chem. A* **2004**, *108*, 9652.

(24) Miasek, P. G.; Harrison, A. G. *J. Am. Chem. Soc.* **1975**, *97*, 714.

(25) Ahmed, M. S.; Dunbar, R. C. *J. Am. Chem. Soc.* **1987**, *109*, 3215.

(26) Barfknecht, A. T.; Brauman, J. I. *J. Chem. Phys.* **1986**, *84*, 3870.

(27) Boering, K. A.; Brauman, J. I. *J. Chem. Phys.* **1992**, *97*, 5439.

(28) Fernandez, A. I.; Viggiano, A. A.; Maergoiz, A. I.; Troe, J.; Ushakov, V. G. *Int. J. Mass Spectrom.* **2005**, *241*, 305.

(29) Viggiano, A. A.; Fernandez, A. I.; Troe, J. *Phys. Chem. Chem. Phys.* **2005**, *7*, 1533.

(30) Arnold, S. T.; Williams, S.; Dotan, I.; Midey, A. J.; Morris, R. A.; Viggiano, A. A. *J. Phys. Chem. A* **1999**, *103*, 8421.

(31) Arnold, S. T.; Dotan, I.; Williams, S.; Viggiano, A. A.; Morris, R. A. *J. Phys. Chem. A* **2000**, *104*, 928.

(32) Hueter, U. Creating an airline to the stars. *Aerospace Am.* **1999**, *37*, 40.

(33) Troe, J. *J. Phys. Chem.* **1983**, *87*, 1800.

(34) Snider, N. *J. Phys. Chem.* **1985,** *89*, 1257.

(35) Hirschfelder, J. O.; Curtiss, C. F.; Bird, R. B. *Molecular Theory of Gases and Liquids*; Wiley: New York, 1964.

(36) Miller, Th. M. In *Handbook of Chemistry and Physics*; Lide, D. R., Ed.; CRC Press: Boca Raton, FL, 2003; Section 10, p 163.

(37) Troe, J.; Ushakov, V. G. *J. Phys. Chem. A* submitted.

(38) *NIST Chemistry Webbook*, Linstrom, P. J.; Mallard, W. G., Eds.; NIST Standard Reference Data Base No 69; NIST: Gaithersburg, MD, 2005; http://webbook.nist.gov.